Applied Catalysis B: Environmental 339 (2023) 123152

Contents lists available at ScienceDirect

Applied Catalysis B: Environmental

journal homepage: www.elsevier.com/locate/apcatb

Coke resistant NiCo/CeO_2 catalysts for dry reforming of methane derived from core@shell Ni@Co nanoparticles

Euiseob Yang [1], Eonu Nam [1], Yoonjeong Jo, Kwangjin An *

School of Energy and Chemical Engineering, and Graduate School of Carbon Neutrality, Ulsan National Institute of Science and Technology (UNIST), Ulsan 44919, the Republic of Korea

ARTICLE INFO

Keywords:
Dry reforming of methane
Nanoparticles
Core@shell Ni@Co
CeO_2
Coking

ABSTRACT

Core@shell Ni@Co and bimetallic alloyed Ni–Co nanoparticles with controlled Co/Ni compositions were prepared and supported on CeO_2 to investigate their performance in catalytic dry reforming of methane (DRM) and occurrence of sintering and coking. Increasing the Co/Ni ratio significantly reduced coke deposition while maintaining catalytic activity for DRM. However, a Co/Ni ratio > 1 caused a rapid decrease in activity. The Ni@Co_1/CeO_2 catalyst exhibited the highest CH_4 and CO_2 conversions, with long-term stability during DRM at 800 °C for 100 h. The initial core@shell structure of the Ni@Co_1/CeO_2 catalyst transformed to a homogeneous alloy after DRM at 800 °C for 10 h, losing its Co shell. However, the bimetallic alloyed Ni–Co_1/CeO_2 catalyst transformed into a non-uniform alloy rich in Co on the surface after DRM for 10 h. As the elemental distribution of the NPs becomes more homogeneous, Ni–Co_1/CeO_2 exhibit similar catalytic activity to Ni@Co_1/CeO_2 after 50 h. The oxygen vacancies on the CeO_2 surface provided oxygen atoms to the Ni surface, removing carbon species deposited and releasing CO. Therefore, Ni@Co_1/CeO_2 catalyst provides excellent catalytic activity and stability due to the rapid formation of a homogenous alloy and the synergistic effect of Co and CeO_2.

1. Introduction

Fossil-fuel-based energy technologies have driven worldwide advancements but simultaneously accelerated global warming through the emission of greenhouse gases [1,2]. Innovative technologies that generate energy with lower atmospheric carbon dioxide (CO_2) emissions are essential to combat global warming and achieve true carbon neutrality. Conversion technologies that use hydrogen (H_2) to replace fossil fuels and utilize CO_2 have recently been proposed as alternatives for energy production, driving the search for clean H_2 productions [3]. Dry reforming of methane (DRM) is an important carbon-neutral process to obtain H_2 and CO from CO_2 and methane (CH_4), two greenhouse gases [4,5]. The syngas (H_2 +CO) generated through DRM can be used in Fischer–Tropsch reactions to generate value-added chemicals, such as olefins, liquid fuels, and aromatics [6,7]. Alternatively, H_2 can be directly used as an energy source.

Current representative highly active DRM catalysts include Rh, Ru, Pt, and Ni metals [8]. Because Ni is a low-cost non-noble metal, it is the main focus of current DRM research [9,10]. In general, DRM requires high temperatures (above 700 °C) because of their high endothermic character and slow kinetics [11]. High-temperature DRMs are accompanied by chronic catalyst deactivation problems such as coke deposition and sintering [12]. Two representative side reactions, the Boudouard reaction ($2CO \rightarrow C + CO_2$) and CH_4 decomposition ($CH_4 \rightarrow C + H_2$), are responsible for carbon deposition on the catalyst surface [13,14]. The high reaction temperatures, over the Tammann temperature of Ni (< 581 °C), causes metal mobility leading to catalytic sintering [15,16].

Several modifications have been developed to improve the stability of Ni catalysts while maintaining their activity [17,18]. Carbon deposition can be prevented by weakening the Ni–C bonds formed in the intermediate step of adsorbing methyl groups, generated by CH_4 activation, onto the catalyst surface. Catalyst stability can be improved by donating oxygen atoms to the catalyst surface, as the oxygen released from the oxide surface reacts with the deposited carbon to release CO [19,20]. The surface properties of Ni catalysts can also be tailored through the incorporation of other metals, improving the DRM activity [21–24]. Ni-based bimetallic structures can be classified as core@shell, random, intermetallic, and single-atom alloys [25–27]. Chen et al. reported a PtNi supported on hydrotalcite catalyst has lower adsorption

* Corresponding author.
E-mail address: kjan@unist.ac.kr (K. An).

[1] These authors contributed equally to this work.

https://doi.org/10.1016/j.apcatb.2023.123152
Received 9 May 2023; Received in revised form 15 July 2023; Accepted 3 August 2023
Available online 12 August 2023

energy for carbon species than monometallic Ni(111) and Pt(111) [28]. The electronic structure of bimetallic PtNi effectively reduced carbon deposition on the catalyst surface. Surface encapsulation in an inorganic shell also prevents coke deposition while improving the thermal stability of the catalyst by acting as an external protective barrier [29–32]. A core@shell structure can be formed by coating the catalyst surface with porous materials such as SiO_2 and Al_2O_3, which reduces the thermal agglomeration of the core Ni catalyst owing to the confinement effect, providing excellent coke resistance in DRM [33–35]. Kosari et al. reported that nickel silicate hollow spheres with thin shell thickness and maximized internal cavity exhibited excellent catalytic activity and coke resistance in DRM [36]. The use of reducible oxide-based supports, such as CeO_2 and TiO_2, with a high density of oxygen vacancies can further reduce carbon species on the Ni surface by supplying oxygen atoms to the metal surface [37,38]. Metal–support interactions in Ni/CeO_2 catalysts can be improved by decreasing the Ni particle size [39]. In addition, the oxygen vacancies on the CeO_2 surface activate CO_2 molecules, improving DRM performance [40–42]. Li et al. reported that a cubic CeO_2 yolk Ni phyllosilicate shell (CeO_2@Ni-Ps YS) catalyst exhibited excellent catalytic performance and stability in DRM due to the sinter resistance and oxygen mobility of CeO_2 [43]. Therefore, an effective DRM catalyst with high structural stability can be developed by introducing an external metal to Ni and selecting an appropriate reducible oxide-based support.

Co, Fe, and Cu are commonly used to modify the electronic and surface properties of Ni [44–47]. The high oxophilicity of Co causes the DRM to occur through a different CH_4 activation pathway; here, CH_4 reacts with oxygen atoms on the Co surface through σ-bond metathesis to form an H_3C–H–O transition state [48]. Ni and Co are advantageous metals for the preparation of bimetallic catalysts because of their similar electronic structures. Bimetallic NiCo catalysts can provide oxygen species to the deposited carbon to accelerate the reaction with higher oxygen affinity. However, the optimal incorporation and distribution of Co in Ni-based catalysts is important. Takanabe et al. reported that a $NiCo/TiO_2$ catalyst exhibited lower CH_4 conversion with increasing Co content in DRM [49]. Cao et al. reported reduced carbon deposition and improved DRM activity by optimizing the thickness of the Co oxide deposited as an atomic layer on the Ni/Al_2O_3 catalyst surface [50]. However, the overcoated Co reduces the activity by masking the active Ni sites, thereby reducing activity. Therefore, more detailed studies are required to optimize the catalytic performance and reduce coke deposition by controlling the thickness of the Co coating on the surface of Ni nanoparticles (NPs) at the nanometer scale.

Bimetallic NPs have recently been produced through well-developed colloidal synthesis to improve catalytic performance and stability. Their chemical, mechanical, and electrical properties are controlled by geometric and bifunctional effects [51,52]. The distribution of foreign atoms such as Co, Fe, and Cu in Ni-based bimetallic NPs and their structures greatly influences their catalytic performance in the DRM. However, Ni-based bimetallic NPs are reconstituted during high-temperature DRM with many gaseous reactants and products (CH_4, CO_2, CO, H_2, and H_2O), completely changing their original structures and distributions. Yan et al. reported the structural evolution of NiCu bimetallic NPs during the DRM using molecular dynamics [53]. Reconstruction of the shape of bimetallic NPs was observed by outward and inward migration of Cu and Ni atoms, respectively. The optimized $94Ni6Cu/Al_2O_3$ catalyst exhibited excellent activity, coke resistance, and extended lifetime because the structural transformation caused the Cu atoms to migrate to the surface. Even if the metal composition and distribution are well controlled during catalyst preparation, it is still difficult to understand how the catalyst is deformed during the DRM and which surface structure and electronic properties cause reduced coking and prevent sintering. When uniformly synthesized bimetallic NPs were applied to the DRM, it was unclear which metal was more abundant on the surface and which metal was the strongest oxidizer. According to recent research, coke deposition is reduced by adding Co to the surface of active Ni species [54]. However, it is unknown whether bimetallic NiCo, in which a small amount of Co is added to Ni, and core@shell Ni@Co NPs, in which a small layer of Co coats the Ni, synergistically combine to form an effective catalyst. Therefore, a systematic study on how the structure of bimetallic alloy and core@shell NPs change during the DRM is required.

In this study, we prepared core@shell Ni@Co_x NPs with various compositions and precisely tuned their Co shell thicknesses to investigate their impact on sintering, coking, and performance in DRM. Uniform Ni NPs with an average diameter of 10 nm were coated with Co shells at Co/Ni ratios of 0.25, 0.5, 1, 2, and 4 to produce Ni@$Co_{0.25}$, Ni@$Co_{0.5}$, Ni@Co_1, Ni@Co_2, and Ni@Co_4 NPs, respectively. The Ni@Co_x NPs were supported on CeO_2 such that the final Ni content of the catalyst was 10 wt%. Randomly alloyed Ni–Co_x NPs with Co/Ni ratios of 0.25, 1, and 4 were also prepared for comparison. The coking behavior of Ni@Co NPs and randomly alloyed NPs during the DRM was assessed, along with the changes in the surface species with the gradual addition of Co to Ni.

2. Experimental section

2.1. Materials

Nickel(II) acetylacetonate (Ni(acac)$_2$, 95 %), cobalt carbonyl ($Co_2(CO)_8$ ≥ 90 % (Co)), cobalt(II) acetylacetonate (Co(acac)$_2$, 97%), oleylamine (70 %), trioctylphosphine (97 %), 1-octadecene (90 %), and cerium(IV) oxide (nanopowder, < 25 nm) were purchased from Sigma-Aldrich. 2-propanol (99.5 %) and *n*-hexane (95 %) were purchased from Samchun Chemicals. All gases, including ultrahigh-purity CH_4 (99.999 %), CO_2 (99.999 %), He (99.999 %), N_2 (99.999 %), and Ar (99.999 %), were provided by the Techno Industrial Gas Company.

2.2. Preparation of monometallic Ni and Co NPs

Monometallic Ni NPs were prepared via thermal reduction in the presence of oleylamine [55]. Briefly, 0.77 g of Ni(acac)$_2$ was dissolved in oleylamine (12 mL) in a 3-neck round-bottom flask. The mixture was degassed at 100 °C for at least 15 min and purged with inert Ar gas. After adding 4 mL of trioctylphosphine, the mixture was heated to 220 °C at a rate of 5 °C•min^{-1}, and the temperature maintained for 2 h. The liquid turned black because of the thermal reduction of Ni(acac)$_2$, indicating the formation of Ni NPs. After cooling to room temperature (25 °C), the mixture was centrifuged and washed four times with 40 mL of a 1:10 mixture of *n*-hexane and 2-propanol. The precipitated Ni NPs were dispersed in *n*-hexane (20 mL).

Similarly, Co NPs were prepared using 0.53 g of $Co_2(CO)_8$ dissolved in *n*-hexane (6 mL) and oleylamine (12 mL) in a 3-neck round-bottom flask under Ar atmosphere. The solution was degassed at 70 °C for 30 min and purged with inert Ar gas. The reaction was performed by heating the solution at 120 °C for 10 min and 180 °C for 1 h. After the reaction, cooling, washing, centrifugation, and redispersion steps were performed as described earlier.

2.3. Preparation of core@shell Ni@Co_x NPs and randomly alloyed bimetallic Ni–Co_x NPs with a controlled Co/Ni ratio

Core@shell Ni@Co_x NPs were synthesized by using a previously reported method, with minor modifications [55]. After the thermal reduction of Ni(acac)$_2$, the Ni NPs were directly used as the core in a continuous reaction with $Co_2(CO)_8$ to generate a core@shell structure. $Co_2(CO)_8$ dissolved in *n*-hexane was directly injected into a flask containing Ni NPs without contact with air. The amount of $Co_2(CO)_8$ was varied as 0.13, 0.26, 0.53, 1.06, and 2.12 g to obtain Ni@Co_x ($x = 0.25$, 0.5, 1, 2, and 4) with different Co/Ni ratios. The *n*-hexane was completely evaporated by degassing at 25 °C for 2 h and at 70 °C for 20 min. The mixture was heated to 120 °C for 10 min and maintained at

180 °C for 1 h to produce Ni@Co_x NPs.

Randomly alloyed bimetallic Ni–Co_x NPs were synthesized by thermal reduction in the presence of both metal acetylacetonate precursors. The relative amounts of the precursors and oleylamine were varied to obtain different Co/Ni ratios. Briefly, $Ni(acac)_2$ (0.77 g) and $Co(acac)_2$ (0.19, 0.77, and 3.08 g for x = 0.25, 1, and 4, respectively) were dissolved in oleylamine (15, 24, and 60 mL for x = 0.25, 1, and 4, respectively) in a round-bottom flask. After degassing, trioctylphosphine (5, 8, and 20 mL for x = 0.25, 1, and 4, respectively) was added, and the solution mixture was heated to 220 °C at a rate of 5 °C•min^{-1} and maintained at that temperature for 2 h. After cooling, the mixtures were washed and redispersed in the same way as the monometallic NPs.

2.4. Preparation of CeO_2-supported NP catalysts

CeO_2 nanopowder (1.5 g) was dispersed in 1-octadecene (40 mL) in a round bottom flask. The prepared NP solution was dispersed in *n*-hexane, sonicated, and added to the flask. The mixture was degassed at 100 °C for 15 min and purged with an inert gas. The mixture was then heated at 200 °C for 30 min. After cooling to 25 °C, the black precipitate formed was collected by centrifugation and washed four times with a mixture of acetone and *n*-hexane. The obtained catalyst was dried in an oven at 60 °C. The Ni loadings of the Ni@Co_x and Ni–Co_x/CeO_2 catalysts were 10 wt% of the support, and the Co loadings of the catalysts with x = 0.25, 0.5, 1, 2, and 4 were 2.5, 5, 10, 20, and 40 wt%, respectively. On the other hand, the loading of monometallic Ni and Co NPs on CeO_2 was 10 wt%.

For comparison, Ni@Co_x NPs supported on SiO_2 (MCF-17) and γ-Al_2O_3 (Puralox SBa 200, Sasol) were prepared in the same way as Ni@Co_1/CeO_2. MCF-17 silica was synthesized by a previously reported literature method [56].

2.5. Catalyst Characterization

Structural characterization of the catalysts was performed by employing transmission electron microscopy (TEM), high-angle annular dark-field scanning transmission electron microscopy (HAADF–STEM), and energy-dispersive X-ray spectroscopy (EDS) using a JEM-2100 F (JEOL) microscope with an acceleration voltage of 200 kV. Inductively coupled plasma optical emission spectroscopy (ICP–OES) was performed on a 700-ES spectrometer (Varian). Thermogravimetric analysis (TGA) of the spent catalysts was performed by using a TGA5500 instrument (TA Instruments). The spent catalyst (10 mg) obtained after the DRM was heated to 800 °C at a rate of 10 °C•min^{-1} with air flow (25 mL•min^{-1}). X-ray diffraction (XRD) spectra were collected from beamline 6D at the Pohang Accelerator Laboratory. H_2-temperature-programmed reduction (H_2-TPR) and CO_2-temperature-programmed desorption (CO_2-TPD) were performed using a BELSORP-max II (MicrotracBEL) analyzer. For H_2-TPR measurements, 50 mg of the catalyst was loaded into a quartz reactor and pretreated at 500 °C for 1 h under He flow (50 mL•min^{-1}). After cooling to 50 °C, the catalyst was stabilized by purging with He for 1 h, and H_2 consumption was monitored by gas chromatography (GC) using a thermal conductivity detector (TCD) by increasing the temperature to 900 °C at a heating rate of 10 °C•min^{-1}. For the CO_2-TPD measurements, 50 mg of the catalyst was loaded into a quartz reactor and reduced at 700 °C for 1 h. The catalyst was purged with He (50 mL•min^{-1}) during cooling to 40 °C. Then, a CO_2/He gas mixture (10 % CO_2, 30 mL•min^{-1}) was introduced and maintained for 1 h. After CO_2 adsorption, the amount of desorbed CO_2 was monitored by GC using a TCD at 600 °C and a heating rate of 10 °C•min^{-1}. X-ray photoelectron spectroscopy (XPS) analysis was performed using an Al Kα X-ray photoelectron spectrometer (Thermo Fisher). Prior to the XPS measurements, the catalysts were reduced by using H_2/Ar flow (4 %, 200 mL•min^{-1}) at 700 °C for 1 h.

2.6. Catalyst evaluation

Catalytic DRMs were performed in a continuous-flow fixed-bed reactor. The catalyst (20 mg) was diluted with 40–60 mesh sieved quartz sand (1 g) and placed in a 10 mm inner diameter quartz tube inside the reactor. After reduction with pure H_2 (50 mL•min^{-1}) at 700 °C for 1 h, feed gases with a CH_4:CO_2:N_2 ratio of 1:1:1 was injected into the reactor at a weight hourly space velocity (WHSV) of 90,000 mL•g_{cat}^{-1}•h^{-1}. The DRM was performed sequentially at different temperatures of 600, 700, 750, and 800 °C. The reaction time was limited to 3 h at each temperature because coke deposition during the reaction caused clogging and a significant drop in pressure. For the catalyst with secured stability, an additional DRM was performed at 800 °C for 100 h. The gaseous products were analyzed by using a YL6500 online GC (Young-In Chromass) with a TCD (Carboxen 1000 column) to detect CH_4, CO_2, H_2, 2. The CH_4 (X_{CH_4}) and CO_2 (X_{CO_2}) conversions and H_2/CO ratio were calculated using the following equations:

$$X_{CH_4}(\%) = \frac{F_{CH_4}{}^{in} - F_{CH_4}{}^{out}}{F_{CH_4}{}^{in}}$$

$$X_{CO_2}(\%) = \frac{F_{CO_2}{}^{in} - F_{CO_2}{}^{out}}{F_{CO_2}{}^{in}}$$

$$H_2 \Big/ \mathrm{CO} = \frac{F_{H_2}{}^{out}}{F_{CO}{}^{out}}$$

where $F_{CO_2}{}^{in}$, $F_{CO_2}{}^{out}$, $F_{CH_4}{}^{in}$, $F_{CH_4}{}^{out}$, $F_{H_2}{}^{out}$, and $F_{CO}{}^{out}$ represent the inward and outward volume flow rates of CO_2, CH_4, H_2, and CO, respectively.

3. Results and discussion

3.1. Preparation of core@shell Ni@Co_x NP CeO_2-supported catalysts

Core@shell Ni@Co NPs were synthesized via a colloidal method under air-tight condition using a Schlenk line. Ni@Co NPs were obtained in a two-step process by synthesizing Ni NPs and then coating their surfaces with Co precursors. Ni NPs with a narrow size distribution (10.1 ± 0.6 nm) were synthesized by thermal reduction of $Ni(acac)_2$ in the presence of oleylamine and trioctylphosphine (Fig. S1). The as-synthesized Ni NPs reacted with the Co precursor $Co_2(CO)_8$ to form Ni@Co NPs. Nucleation of the Co precursor must be avoided to obtain monodispersed Ni@Co NPs [55,57]. Because $Co_2(CO)_8$ is a galvanically inert precursor with zero-valent Co^0, no Ni metal was released from the Ni NPs. Therefore Ni@Co NPs were formed while maintaining the Co/Ni ratio. Ni@Co_x (x = 0.25, 0.5, 1, 2, and 4) NPs with controlled thickness and concentration of the Co shell were prepared by fixing the amount of Ni NPs and adjusting the relative amount of $Co_2(CO)_8$ to 0.25, 0.5, 1, 2, and 4. Co NPs were prepared using the same process but without Ni NPs (Fig. S2).

TEM images of Ni@$Co_{0.25}$, Ni@Co_1, and Ni@Co_4 NPs are shown in Fig. 1a–c. The Co shell thickness of the Ni@Co_x NPs increased with an increase in Co content. The average diameters of Ni@$Co_{0.25}$, Ni@Co_1, and Ni@Co_4 were 11.7, 12.9, and 15.6 nm, respectively. HAADF–STEM images and the corresponding EDS mapping confirmed the presence of Ni@Co_x NPs with a controlled Co content (Fig. 1d–f and S3). All Ni@Co_x NPs had a distinct core@shell morphology, without any individual NPs (Fig. S4). The Co content was proportional to the ratio x of the Ni@Co_x NPs. The synthesized Ni, Co, and Ni@Co_x NPs were supported on CeO_2, a reducible support. The prepared NPs were successfully deposited on CeO_2, as confirmed in EDS mapping (Fig. S5). The Ni loading of Ni@Co_x/CeO_2 and Ni/CeO_2 were fixed at 10 wt% and the catalyst was synthesized accordingly (Fig. 1g). The Co/Ni ratio of all catalysts was confirmed by ICP–OES measurements (Table S1).

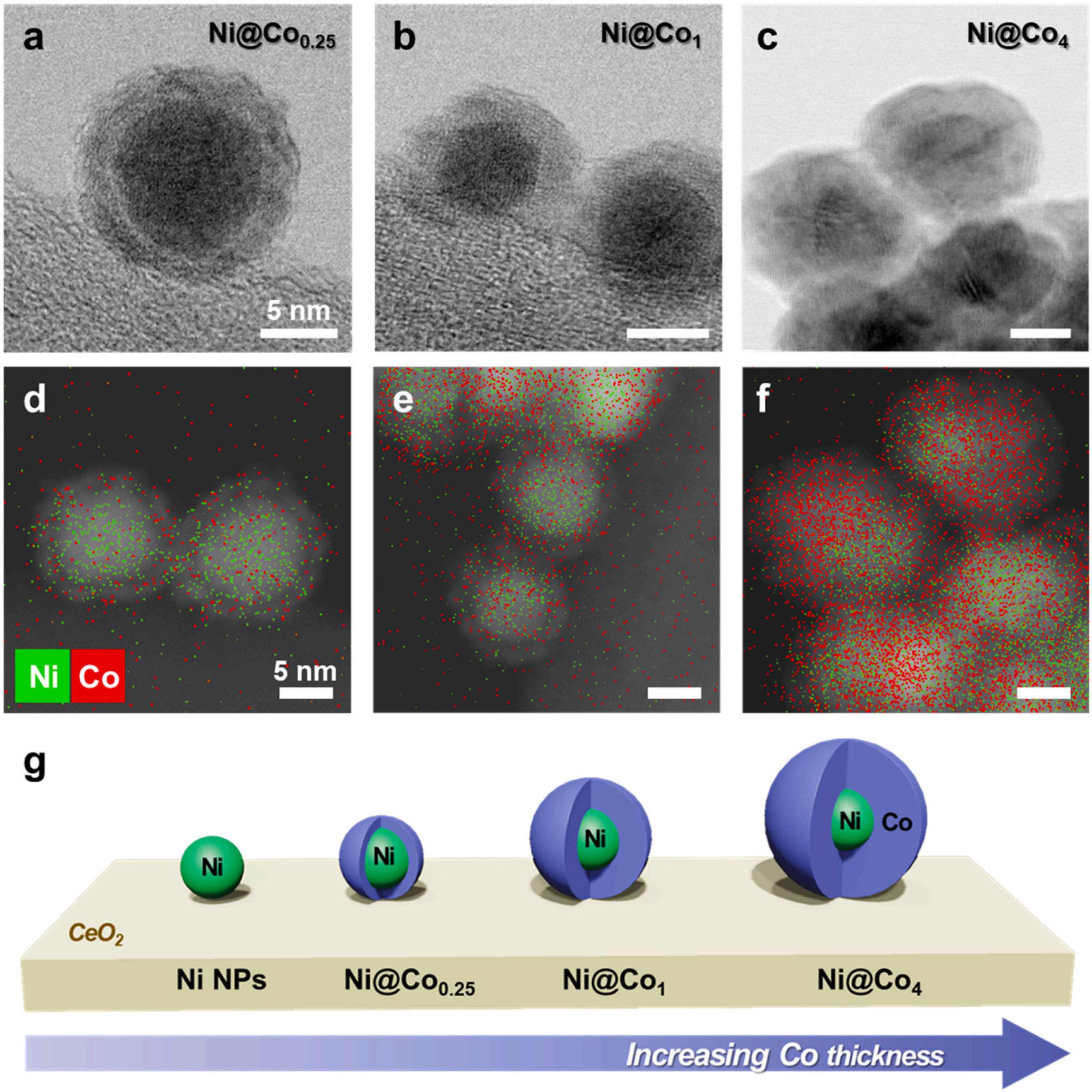

Fig. 1. (a–c) TEM images and (d–f) corresponding EDS mapping of core@shell Ni@Co_x NPs with controlled Co composition ($x = 0.25$, 1, and 4) and shell thickness. All scale bars represent 5 nm. (g) Schematic illustration of the core@shell Ni@Co_x NPs with controlled Co thicknesses on Ni NPs.

3.2. Catalytic performance and stability for DRM

The catalytic activity and stability of CeO_2-supported Ni, Co, and Ni@Co_x NP catalysts in the DRM were investigated (Fig. 2). The DRM was performed with a gradual increase in reaction temperature from 600 to 800°C. Average CH_4 and CO_2 conversions using Co/CeO_2, Ni/CeO_2, and Ni@Co_x/CeO_2 are depicted in Figs. 2a and 2b, respectively. As shown in Fig. 2, the catalytic activity of Ni/CeO_2 was maintained or reduced by the introduction of Co. The Ni@Co_x/CeO_2 catalysts with Co/Ni ratios of ≤ 1 showed similar CH_4 and CO_2 conversions. The H_2/CO ratio showed a similar trend to that of the CH_4/CO_2 conversion owing to the correlation between the thermodynamic equilibrium of the DRM and the H_2/CO ratio (Fig. 2c). CeO_2-supported Ni, Ni@$Co_{0.25}$, Ni@$Co_{0.5}$, and Ni@Co_1 catalysts exhibited much higher conversions regardless of reaction temperature than monometallic Co and Co-rich catalysts. Based on this result, it is expected that a sufficient amount of Ni will be exposed on the NP surface of the Ni@Co_x/CeO_2 ($x = 0.25$, 0.5, and 1) during the DRM. However, the Ni and Ni@$Co_{0.25}$ catalysts showed rapid decrease in activity over time at high temperatures (750 and 800 °C), and the Ni@$Co_{0.5}$ and Ni@Co_1 catalysts showed higher and more stable activity. This difference is closely related to the coke resistance and sintering of the catalyst. The overall CO_2 conversion was higher than the CH_4 conversion and the H_2/CO ratio was less than 1 for all catalysts. This is because the reverse water gas shift reaction ($CO_2 + H_2 \rightarrow CO + H_2O$) occurs during DRM [58,59].

The stability of a series of Ni@Co_x/CeO_2 catalysts was evaluated by

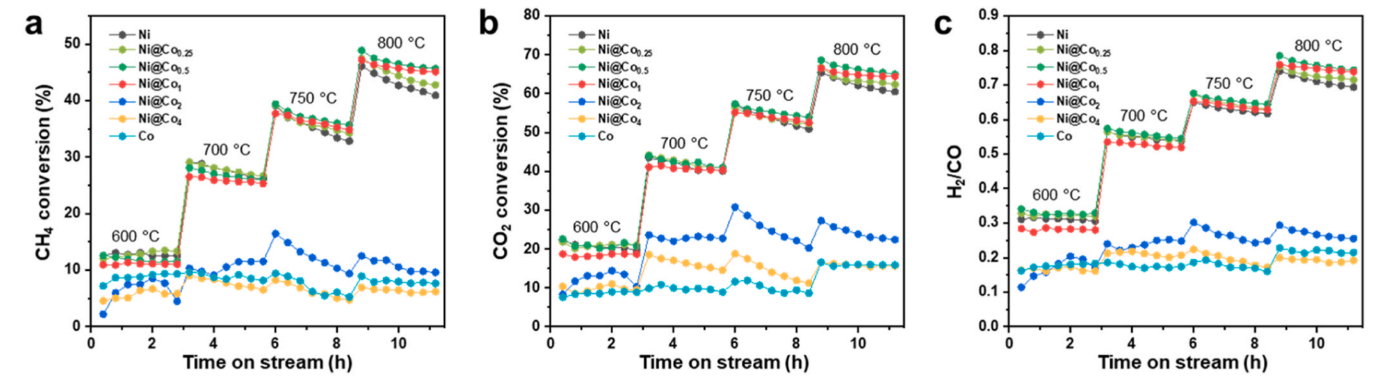

Fig. 2. (a) CH_4 conversion, (b) CO_2 conversion, and (c) H_2/CO ratio for DRM over $Ni@Co_x/CeO_2$ catalysts with different Co/Ni ratios. The DRM was sequentially performed at 600, 700, 750, and 800 °C for 3 h, respectively. Other reaction conditions were 1 bar, WHSV of 90,000 $mL\bullet g_{cat}^{-1}\bullet h^{-1}$, and $CH_4/CO_2/N_2$ of 1:1:1.

conducting TGA. After DRM, the amount of coke deposited on the spent catalyst was estimated by TGA (Fig. 3a). CeO_2-supported $Ni@Co_1$, $Ni@Co_2$, $Ni@Co_4$, and Co NP catalysts showed coke resistance without significant weight loss up to 800 °C. However, coke formation on the catalyst surface gradually increased when the Co/Ni ratio was < 1. The spent CeO_2-supported $Ni@Co_{0.5}$, $Ni@Co_{0.25}$, and Ni NP catalysts exhibited weight losses of 11 %, 27 %, and 31 %, respectively. The TGA results also show weight gain due to metal oxidation under an air flow condition. The weight gain shown in TGA is obvious for catalysts with higher Co contents than Ni. For $Ni@Co_x$ catalysts with lower Co content than Ni, the weight loss due to coke removal is dominant and the weight gain by metal oxidation is negligible. The derivative thermogravimetric (DTG) profiles of the coke deposited spent catalysts show distinct coke oxidation profiles as a function of temperature (Fig. 3b). The endothermic peak maxima were observed at 665, 609, and 566 °C for Ni, $Ni@Co_{0.25}$, and $Ni@Co_{0.5}$, respectively. A characteristic DTG peak appeared in the low-temperature region with increasing Co loading, indicating that more reactive carbon species were deposited on the surface. The initial high DRM activity of Ni/CeO_2 catalysts originating from the Ni surface abruptly decreased by severe coke deposition. This problem was significantly mitigated by introducing Co shell to the Ni NPs, but the catalytic activity decreased by more than half as the Co/Ni ratio exceeded 1. As a result, only $Ni@Co_1/CeO_2$ among the $Ni@Co_x/CeO_2$ catalysts exhibited excellent activity and stability. To confirm the long-term durability of $Ni@Co_1/CeO_2$, DRM was performed on this catalyst at 800 °C for 100 h. Fig. 3c shows that the catalytic activity was maintained without abrupt decrease.

3.3. Characterization of $Ni@Co_x/CeO_2$ catalysts

The spent $Ni@Co_x/CeO_2$ catalysts were structurally characterized using TEM to investigate the relationship between the thickness of the Co shell and coke deposition after the DRM (Fig. 4). The TEM result displays that all $Ni@Co_x$, Ni, and Co NP catalysts are sintered with agglomerated NPs in the harsh reaction environment. The CeO_2-supported Ni, $Ni@Co_{0.25}$, and $Ni@Co_{0.5}$ NP catalysts produced carbon nanotubes during the DRM (Fig. 4a–c). However, no coke deposition was observed in spent $Ni@Co_1$, $Ni@Co_2$, $Ni@Co_4$, and Co catalysts (Fig. 4d–g), which is consistent with the TGA results (Fig. 3a). The addition of Co to Ni NPs considerably mitigated the coke deposition, and significant coke resistance was observed for the $Ni@Co_x/CeO_2$ with Co/Ni ratios ≥ 1. The spent CeO_2 supported $Ni@Co_1$, $Ni@Co_2$, and $Ni@Co_4$ catalysts without coke deposition contained alloy NPs with uniformly distributed Ni and Co (Fig. S6). However, severe catalyst aggregation occurred when using only the Co/CeO_2 catalyst in the DRM (Fig. 4g).

The structural changes of $Ni@Co_x$ NPs were investigated from the XRD patterns of the as-prepared and reduced $Ni@Co_x/CeO_2$ catalysts (Fig. 5). All as-prepared catalysts exhibited only a fluorite CeO_2 structure, With XRD peaks at 28.6°, 33.1°, 47,4°, 56.2°, 59.5° 69.3°, 76.7°, 79.2°, 88.5°, and 95.4° corresponding to the (111), (200), (220), (311), (222), (400), (331), (422), (420), and (511) planes of CeO_2, respectively (JCPDS, No. 34-0394). No Ni- or Co-related XRD peaks were observed because the highly dispersed $Ni@Co_x$ NPs on CeO_2 (Figs. 5a and 5b). New peaks originating from Ni and Co were observed for the reduced $Ni@Co_x/CeO_2$ catalysts after reduction at 700 °C for 1 h (Fig. 5c). The sharp XRD peaks of the reduced and spent catalysts indicated that the NP size increased after the reduction. The metallic phases of Ni and Co were virtually indistinguishable because of their similar fcc structures. XRD

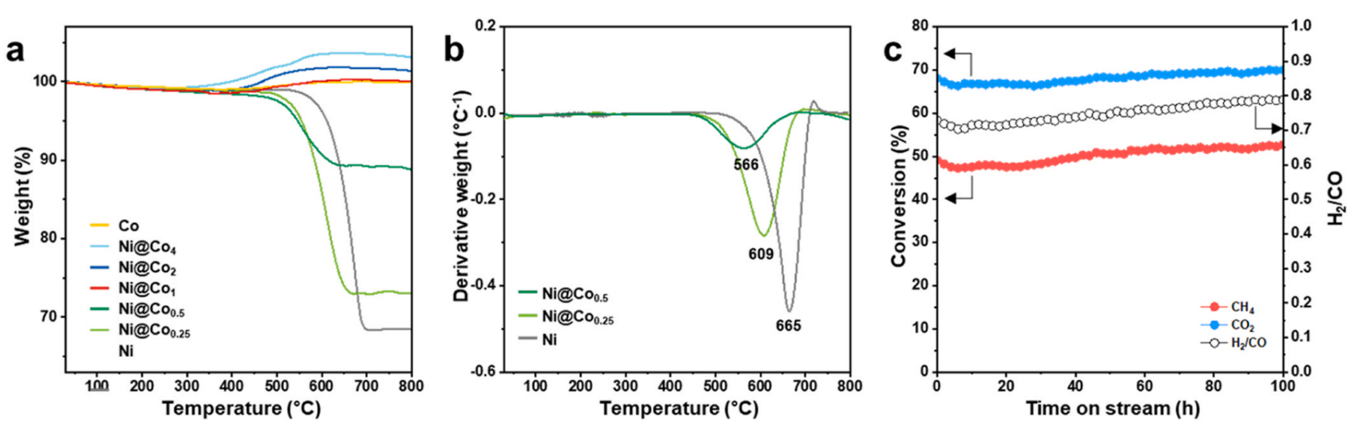

Fig. 3. (a) TGA and (b) DTG profiles of the spent $Ni@Co_x/CeO_2$ catalysts after DRM. (c) CH_4 conversion, CO_2 conversions, and H_2/CO ratio of the $Ni@Co_1/CeO_2$ catalyst during DRM at 800 °C for 100 h.

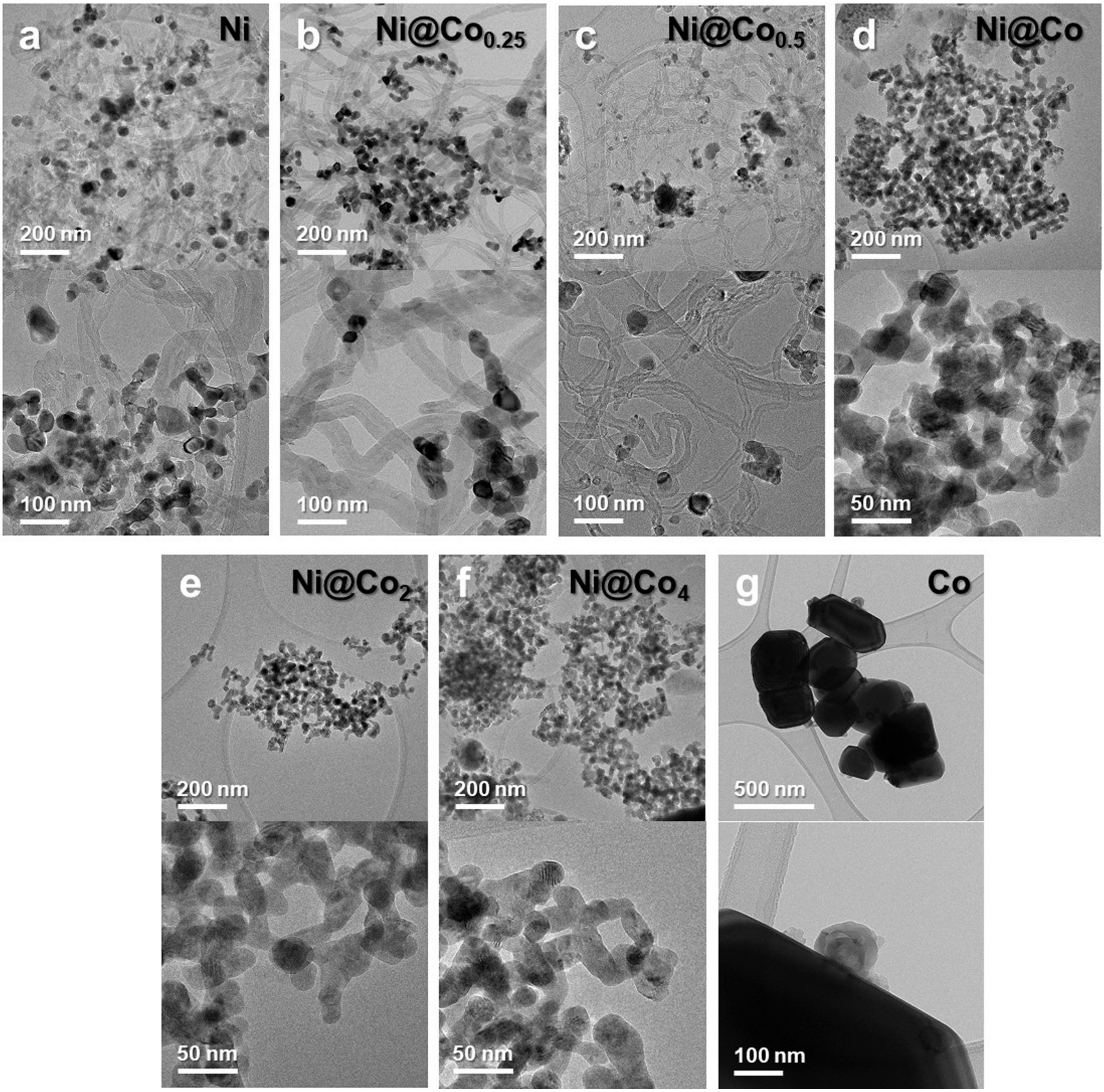

Fig. 4. TEM images of spent (a) Ni/CeO_2, (b–f) $Ni@Co_x/CeO_2$, and (g) Co/CeO_2 catalysts with different Co/Ni ratios after the DRM.

peaks were observed at 44.5°, 51.8°, 76.4°, and 92.9° for Ni (JCPDS, No. 04-0850), and at 44.2°, 51.5°, 75.8°, and 92.3° for Co, corresponding to the (111), (200), (220), and (311) planes of the fcc structures (JCPDS, No. 15-0806), respectively. Fig. 5d shows XRD peaks of the reduced $Ni@Co_{0.5}$, $Ni@Co_1$, and $Ni@Co_2$ catalysts at 44.38°, 44.32° and 44.24° respectively, which are located between the peaks of metallic Co and Ni. As the content of Co increases, the peak of the metal shifts to a lower position, indicating the formation of a Ni_xCo_y alloy and the finely tuned chemical composition [60]. In addition, the lattice parameters of Ni for the reduced catalyst were calculated to be 3.533, 3.537, and 3.543 Å, respectively. From these results, it was confirmed that the thicker the Co shell, the more Co was incorporated into the Ni lattice after reduction pretreatment.

H_2-TPR was performed to investigate the specific interactions of Ni, Co, and CeO_2 in $Ni@Co_x/CeO_2$ catalysts as a function of Co content (Fig. 6a). The H_2-TPR peaks of Ni/CeO_2 at 265 and 460 °C are attributed to the reduction of chemisorbed oxygen species at oxygen vacancies in CeO_2 (α) and well-dispersed NiO on CeO_2 (β), respectively [46,61]. Prior to H_2-TPR measurement, a catalyst in a form of Ni NPs surrounded by Co was pretreated at 500 °C for 1 h under He flow. During this process, elemental diffusion occurs in the $Ni@Co_x$ NPs, exposing Ni to the particle surface. The α peak shifts to higher temperatures and decreases in intensity as the Co content increases from Ni to $Ni@Co_1/CeO_2$ catalyst. A previous study reported that Ni^{2+} can be incorporated into the CeO_2 lattice to form a Ni–Ce–O solid solution, generating oxygen vacancies and reducible oxygen species [62]. The rich Ni–Ce–O interfacial sites make it easier to remove adsorbed oxygen by H_2 [63,64]. The total amount of Ni exposed to the particle surface inevitably decreases as the thickness of the Co shell makes it difficult to expose the Ni. Therefore, the Ni–Ce–O interfacial sites decrease with increasing Co content and

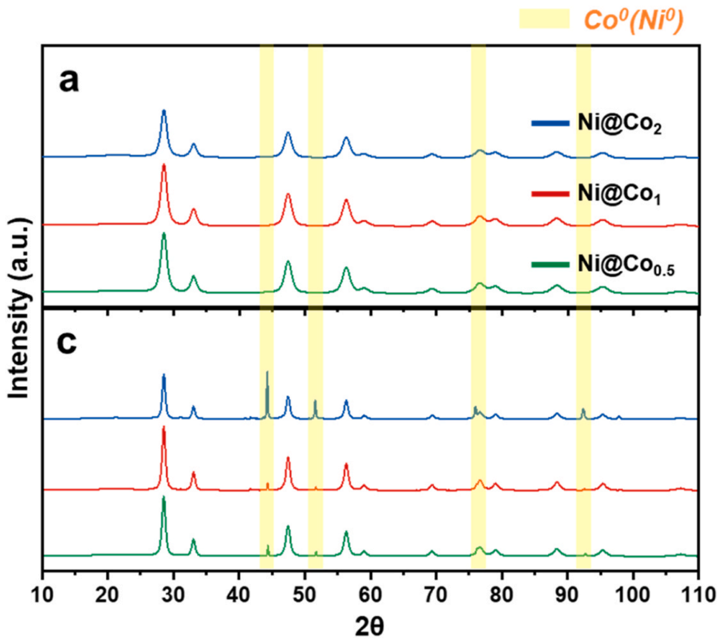

Fig. 5. XRD patterns of (a) as-prepared, (c) reduced Ni@Co_x/CeO_2 catalysts ($x = 0.5$, 1, and 2). Magnified XRD patterns of the (b) as-prepared and (d) reduced catalysts ranges of 43–45°.

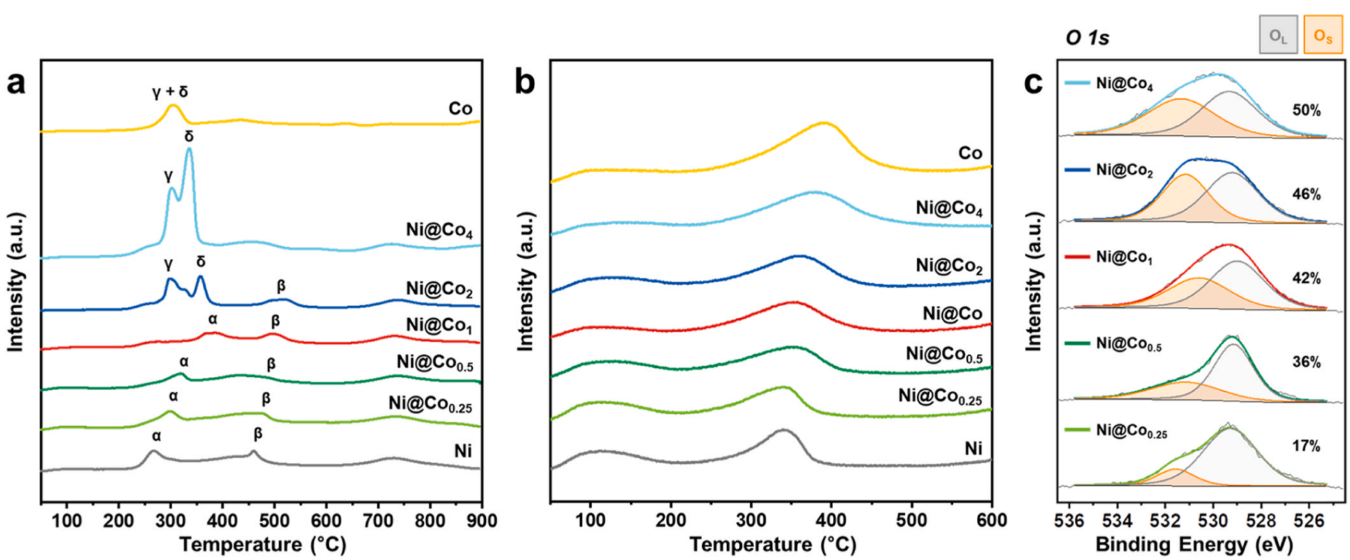

Fig. 6. (a) H_2-TPR and (b) CO_2-TPD profiles and (c) the O 1 s XPS spectra of Ni@Co_x/CeO_2 catalysts. The orange and gray line spectra were obtained via decomposition into linear combinations corresponding to surface oxygen (O_S) and lattice oxygen (O_L), respectively.

the α peak shift to higher temperatures. Similarly, the β peak also shifts to the higher temperature with increasing Co content, due to the increased Ni dispersion. However, a further increase in Co content, seen in the Ni@Co_2 and Ni@Co_4 catalysts, resulted in different H_2-TPR profiles owing to the change in the surface properties of Ni@Co_x NPs, which were much closer to those of monometallic Co catalysts. For example, the H_2-TPR profile of Ni@Co_2/CeO_2 differed from that of Ni@Co_1/CeO_2 (Fig. 6a). The H_2-TPR profile of Co/CeO_2 shows a two-step reduction process, from Co_3O_4 to CoO (γ) and finally to Co (δ) [65,66]. In addition, Ni@Co_2 and Ni@Co_4 do not show an α peak unlike other Ni@Co_x catalysts. Based on these results, it was confirmed that the Ni–CeO_2 interaction became stronger as the β peak shifts to higher temperatures, but the α peak disappeared in Ni@Co_2 and Ni@Co_4. The rapid decrease in Ni–Ce–O site for Ni@Co_2 and Ni@Co_4 catalysts shows a similar trend to the decrease in activity of these catalysts (Fig. 2). Therefore, the interactions between Ni or Co metals and the CeO_2 support in Ni@Co_x/CeO_2 catalysts were highly dependent on the Co content.

The CO_2 affinity of the catalyst is essential for DRMs because CO_2 reacts with activated CH_4 and improves catalyst stability by providing oxygen atoms to the deposited coke. CO_2-TPD were performed to determine the basicity of the Ni@Co_x/CeO_2 catalysts. Fig. 6b shows the CO_2 desorption profiles obtained after reduction at 700 °C. The position of the maximum peak for each catalyst was considered to be in the 300–400 °C range, corresponding to the medium base region on the catalyst surface [67,68]. The CO_2 desorption temperature increased with increasing Co/Ni ratio in Ni@Co_x/CeO_2 catalysts. Peaks corresponding to CO_2 desorption were observed at 342, 344, 351, 356, 362, 380, and 393 °C for Ni, Ni@$Co_{0.25}$, Ni@$Co_{0.5}$, Ni@Co_1, Ni@Co_2, Ni@Co_4, and Co catalysts, respectively. Because the oxygen vacancies in CeO_2 are the main agents responsible for CO_2 adsorption, CO_2

desorption did not vary significantly with the adsorption capacity of the catalyst. Therefore, Co metal was the main contributor to the improved CO_2 adsorption on CeO_2. The dynamic adsorption and desorption of CO_2 activated the continuous-flow DRM at 700 °C. The improved surface basicity owing to the addition of Co improved the coke resistance of the Ni@Co_x/CeO_2 catalysts, as confirmed by the TGA and TEM results (Figs. 3a and 4).

XPS spectra of a series of Ni@Co_x/CeO_2 catalysts were collected after reduction at 700 °C. The oxidation states of Ni, Co, and Ce did not change significantly with the Co/Ni ratio (Fig. S7). Fig. 6c shows two deconvoluted peaks at 529 and 531.5 eV corresponding to lattice oxygen (O_L) and surface oxygen (O_S), respectively [69]. The O_S ratio, calculated as $O_S/(O_S + O_L)$, increased with increasing Co/Ni ratio. The O_S ratios of Ni@$Co_{0.25}$, Ni@$Co_{0.5}$, Ni@Co, Ni@Co_2, and Ni@Co_4 were 17 %, 36 %, 42 %, 46 %, and 50 %, respectively. It was reported that Ni–Co alloys strongly adsorb O species due to the high oxygen affinity of Co [70]. However, we found that there was no correlation between the $Ce^{3+}/(Ce^{3+}+Ce^{4+})$ ratio and the Co content (Fig. S7c). The $O_s/(O_s + O_L)$ ratio increased because the increase in Co content induced adsorption of more oxygen species, rather than a numerical change in the lattice oxygen of CeO_2. For higher amounts of surface oxygen, CO is preferably generated via oxidation of coke deposited on the catalyst surface during the DRM. However, excessive addition of Co induces a decrease in surface exposure of Ni, which reduces catalytic activity. Therefore, Ni@Co_1/CeO_2 with the same Ni and Co content is the optimal catalyst with excellent DRM activity and coke resistance. (Figs. 2 and 3a).

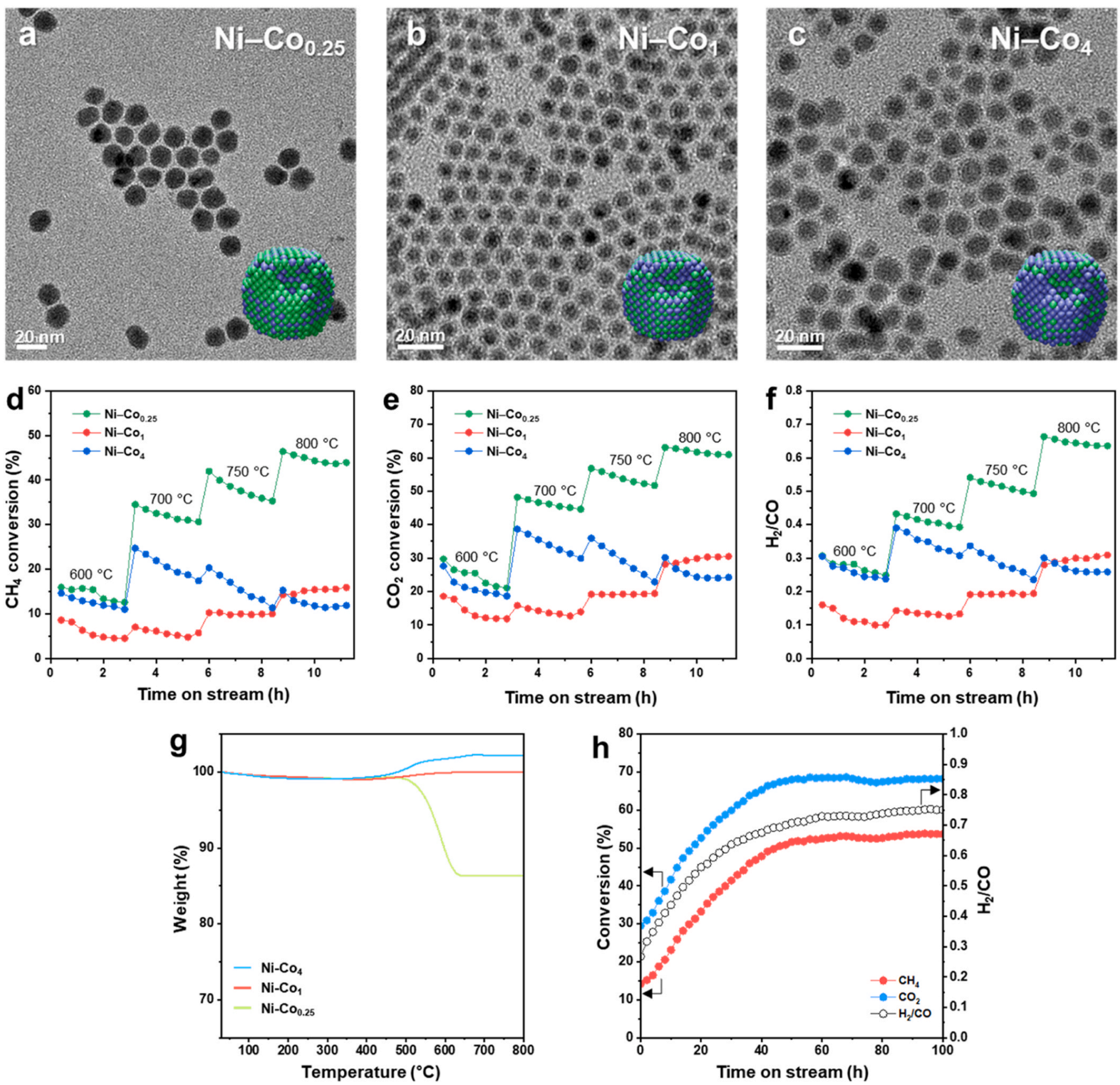

Fig. 7. (a–c) TEM images of as-synthesized randomly alloyed Ni–Co_x NPs with controlled Co composition ($x = 0.25$, 1, and 4). (d) CH_4 conversion, (e) CO_2 conversion, and (f) H_2/CO ratio for DRM over Ni–Co_x/CeO_2 catalysts. The DRM was sequentially performed at 600, 700, 750, and 800 °C for 3 h, respectively. Other reaction conditions were 1 bar, WHSV of 90,000 mL•g_{cat}^{-1}•h^{-1}, and $CH_4/CO_2/N_2$ of 1:1:1. (g) TGA curves of the spent Ni–Co_x/CeO_2 catalysts after the sequential DRM. (h) CH_4 conversion, CO_2 conversion, and H_2/CO ratio of Ni–Co_1/CeO_2 during DRM at 800 °C for 100 h.

3.4. Randomly alloyed bimetallic Ni–Co_x/CeO_2 NP Catalysts

Randomly alloyed bimetallic Ni–Co NPs were synthesized by reacting Ni(acac)$_2$ and Co(acac)$_2$ in oleylamine–trioctylphosphine solution (Fig. 7a–c). Ni–Co_x NPs ($x = 0.25$, 1, and 4) were formed by adjusting the Co precursor by factors of 0.25, 1, and 4, respectively (Fig. S8). The resulting Ni–Co_x NPs were deposited on CeO_2, in the same way as the Ni@Co_x NPs. The prepared randomly alloyed bimetallic Ni–Co_x/CeO_2 catalysts exhibit different DRM performance compared to core shell Ni@Co_x/CeO_2 catalysts with the same Co/Ni ratio. Fig. 7d–f show that Ni–$Co_{0.25}$ exhibits the highest activity regardless of temperature, but Ni–Co_1 shows significantly lower DRM activity than Ni@Co_1 at all temperatures (Figs. 2 and 7). This is presumed to be due to the difference in Ni content exposed to the surface during DRM. TGA profiles of the spent bimetallic Ni–Co_x/CeO_2 catalysts show no weight loss for the Ni–Co_1 and Ni–Co_4/CeO_2 catalysts (Fig. 7g). This is consistent with the TEM analysis (Fig. S9). As shown in Figs. 2 and 7, Ni@Co_x and Ni–Co_x catalysts with Co/Ni greater than 1 showed significantly low DRM activity. The activity of these catalysts did not improve with increasing reaction temperature despite the absence of coke deposition (Fig. 3a). This indicates that deactivation of these catalysts is due to metal oxidation by excess Co on the particle surface during DRM [71]. The excess O adatoms generated in this process cover the metal surface to inhibit DRM. In order to compare with Ni@Co_1/CeO_2, a long-term DRM was conducted using the Ni–Co_1/CeO_2. The Ni@Co_1/CeO_2 catalyst showed long-term durability without significant deactivation during DRM at 800 °C for 100 h, whereas the DRM activity of the Ni–Co_1/CeO_2 catalyst increased gradually over time and stabilized after 50 h (Figs. 3c and 7 f). The Ni and Co content of the alloy NPs is the same as that of the Ni@Co_1/CeO_2 catalyst. Therefore, it is expected that a small amount of Ni is exposed on the particle surface of the Ni–Co_1/CeO_2 catalyst at the beginning of the DRM, and the amount of exposed Ni gradually increases over time.

3.5. Structural changes in NP catalysts

To investigate the difference in catalytic activity for long-term DRM at 800 °C between Ni@Co_1 and Ni–Co_1/CeO_2, elemental distribution analysis was performed on as prepared, reduced, and spent catalysts after DRM for 1 and 10 h. As shown in Fig. S10, the elemental distribution of the NPs from the EDS mapping images of the two spent catalysts (10 h) cannot be compared numerically. Instead, EDS line scanning data of the core@shell and randomly alloyed bimetallic NPs reveal structural changes before and after reduction as well as after the DRM (Fig. 8). The as-prepared Ni@Co_1/CeO_2 catalyst exhibits a Ni core surrounded by a Co shell, as shown in Fig. 8a. Only the Co shell is observed in the region between two NPs (yellow line), with no Ni traces. The well-defined core@shell structure of the Ni@Co_1 NPs lost its original shape

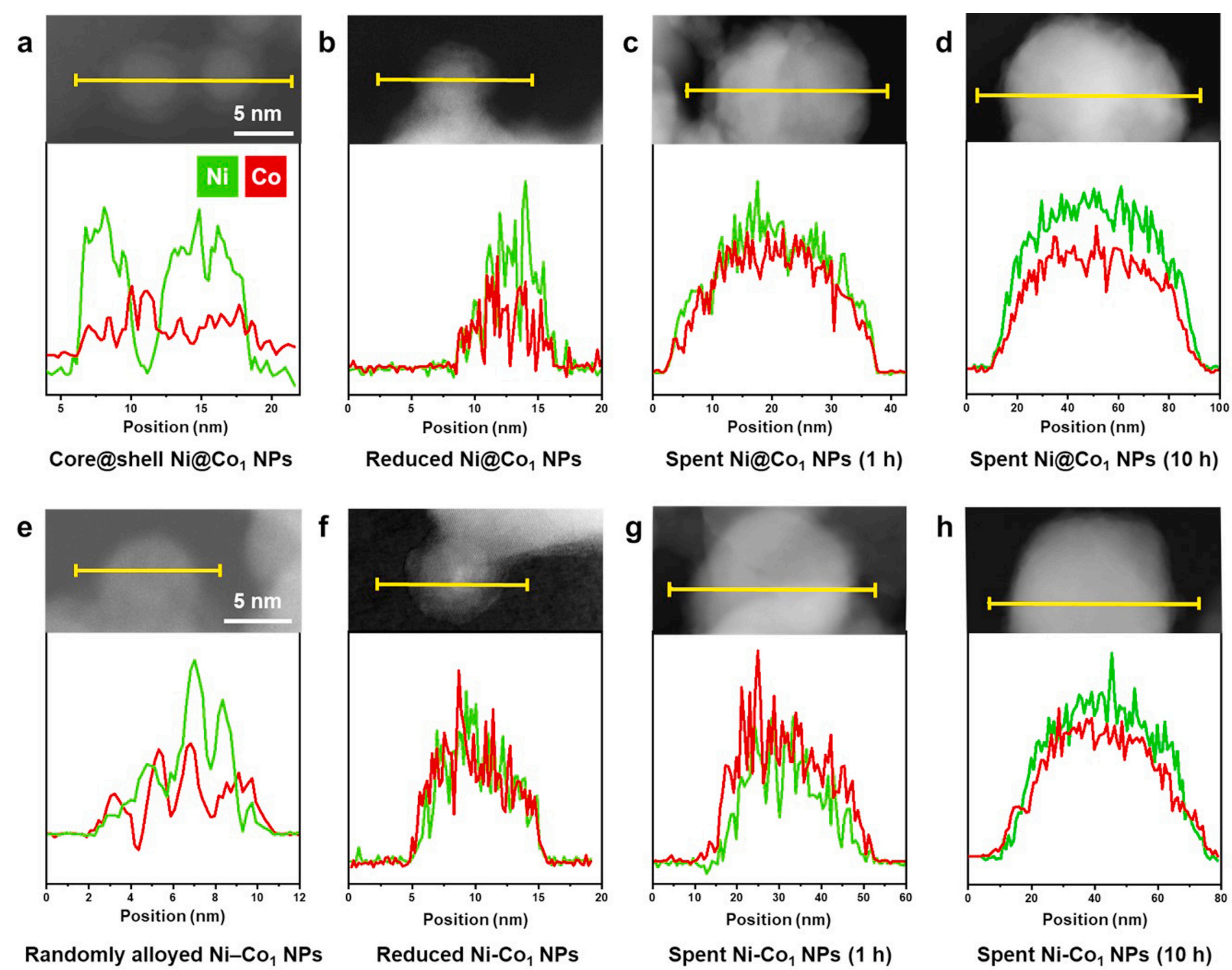

Fig. 8. HAADF-STEM and EDS line mapping images of as-prepared, reduced, and spent (a–d) core@shell Ni@Co_1/CeO_2 and (e–h) bimetallic Ni–Co_1/CeO_2 catalysts. The reduced catalysts were prepared by H_2 reduction at 700 °C for 1 h and the spent catalysts by DRM at 800 °C for 1 and 10 h.

after H_2 reduction at 700 °C for 1 h (Fig. 8b). The Ni and Co distribution of NPs gradually becomes homogeneous after DRM for 1 and 10 h (Figs. 8c and 8d). Based on these results, the $Ni@Co_1/CeO_2$ catalyst is expected to maintain its catalytic activity during the long-term DRM because the NPs were transformed into a homogenous alloy with high Ni content on the surface within 10 h. HADDF-STEM images of the reduced and spent (10 h) $Ni@Co_1/CeO_2$ catalysts also show that the reduced $Ni@Co_1/CeO_2$ NPs had a trace amount of Co shell and the core@shell structure was completely destroyed after DRM for 10 h, turning into alloy NPs (Fig. S11). The elemental composition, determined by EDS mapping and point analysis, showed that the spent $Ni@Co_1/CeO_2$ after DRM for 10 h had a uniform Co/Ni ratio of 0.90–1.09 regardless of location (Fig. S12). In contrast, the as-prepared $Ni–Co_1/CeO_2$ catalysts exhibit NPs with non-uniform distributions of Ni and Co (Fig. 8e). Interestingly, these randomly alloyed NPs became homogeneous after reduction pretreatment, but the Co distribution on the particle surface increased after DRM for 1 h (Figs. 8f and 8g). After DRM for 10 h, the distribution of Ni on the particle surface increased, but the distribution of Co was still dominant. Due to this change in the surface distribution of the NPs, the catalytic activity was gradually increase over time (Fig. 8f). Therefore, we expected that the $Ni-Co_1$ NPs also gradually become a uniform alloy, but the transformation proceeds more slowly than the $Ni@Co_1$ NPs. Due to change in the surface distribution of the NPs, the catalytic activity can gradually increase over time (Fig. 7 f). Similarly, Wu et al. reported that the surface of the NiCo alloy changes uniformly from the Co-rich as the reaction temperature of DRM increases [72]. Wang et al. reported that the Co distribution on the surface of Co@Ni NPs increases with increasing temperature [73]. Based on the decrease in Co distribution on the particle surface during DRM, it can be expected that a higher amount of Co is distributed inside the as-synthesized alloy NPs than outside. This is consistent with the EDS line-scanning results in Fig. 8e. Based on these previous studies, we found that the NiCo bimetallic NPs eventually have a uniform distribution during high-temperature DRM.

The deformation of the NPs during DRM occurred due to the diffusion of Ni and Co inside the particles. In order to have a uniform distribution, diffusion occurs from a space with a large amount of a particular substance to a space with a small amount. In Ni@Co NPs, Ni diffuses outward and Co diffuses inward, while irregular diffusion occurs in random directions in Ni–Co NPs. The two NPs of both catalysts eventually become homogeneous alloys and reach an equilibrium during DRM. Since the diffusion of $Ni@Co_1$ NPs occurs regularly in a specific direction, it is advantageous for the rapid formation of a homogenous alloy. For this reason, unlike $Ni@Co_1$, the $Ni–Co_1$ catalyst represented low activity from the beginning of the long-term DRM (Figs. 3c and 7 h). Based on previous studies and our results, it is concluded that the homogeneous NiCo alloy is in a stable state with low surface energy during DRM. Our results on DRM activity and line scanning show that the $Ni@Co_1/CeO_2$ catalyst is superior to the $Ni–Co_1/CeO_2$ catalyst. From the beginning of the DRM, a sufficient amount of Ni is exposed on the particle surface of $Ni@Co_1/CeO_2$, and a uniform alloy is quickly formed, ensuring excellent catalytic activity and stability.

3.6. The promoting effects of Co and CeO_2

Additional Co-stabilized Ni NPs created Co–Ni bimetallic catalysts with reduced carbon accumulation during DRM. Previous studies have shown that composite Co/Ni alloy catalysts reduce the size of continuous Ni domains and limit the growth of carbon whiskers owing to their low carbon solubility and the carbon adsorption strength of Co [74]. Severe catalyst deactivation was observed during the DRM using CeO_2-supported Ni NPs. However, the use of alternative supports, such as Al_2O_3 or SiO_2, significantly decreased CH_4 and CO_2 conversions in the 600–800 °C temperature range. (Fig. S13a). The Al_2O_3 and SiO_2 supported $Ni@Co_1$ NPs showed severe aggregation, but no coke was observed due to low DRM activity (Figs. S13b and S14). On the other hand, CeO_2 promotes a strong interaction with metals due to its abundant oxygen vacancies [75,76]. Previous studies have shown that the Oxygen vacancies in CeO_2 activate CO_2 molecules during the DRM. In DRMs, an active carbon species (C*) is first generated by removing -H from CH_4 (Scheme 1). Ni is an efficient catalyst for CH_4 activation; however, its deactivation by coke deposition is unavoidable in high-temperature DRMs. The addition of Co to Ni catalysts improves CO_2 activation to form CO and adsorbed oxygen atoms (O_{ads}). CO is produced by combining O_{ads} and CH_x*. CO_2 activation can be further improved by the addition of CeO_2, because its oxygen vacancies generate C–O or formate intermediates via continuous CO_2 adsorption. Coke can form on the Ni surface by the continuous deposition of carbon originating from CH_4. Although C* is generated from CH_4 on the Ni surface, it reacts with O_{ads} provided by the CeO_2 surface, reducing coking. Therefore, CeO_2 and Co both play important roles in preventing coke deposition by generating CO.

The $Ni@Co_x/CeO_2$ catalysts showed better DRM activity than Ni for Co/Ni ratios ≤ 1. The interaction between Ni and the CeO_2 support in $Ni@Co_x/CeO_2$ catalysts was highly dependent on the Co content. The interaction between Ni and CeO_2 becomes stronger with increasing Co content. As the Co content increased above the Ni content, reduction properties similar to monometallic Co catalyst occurred. As the amount of Co in the $Ni@Co_x/CeO_2$ catalyst increases, the number of surface oxygen species increases, resulting in improved coking resistance. However, when the Co content exceeds Ni, the catalytic performance deteriorates due to the increase of oxygen adatoms on the metal surface. Compared to the $Ni@Co_1/CeO_2$, the $Ni–Co_1/CeO_2$ catalyst exhibited much lower activity at the beginning of the long-term DRM due to the formation of a non-homogeneous alloy with a co-rich surface. On the other hand, the NPs of the $Ni@Co_1/CeO_2$ catalyst are advantageous for elemental diffusion due to their ordered core@shell structure. As a result, a uniform alloy was quickly formed on this catalyst, showing stable and excellent activity from the beginning of long-term DRM.

4. Conclusion

Core@shell-typed $Ni@Co_x$ NPs with controlled Co/Ni compositions of 0.25, 0.5, 1, 2, and 4 were prepared to investigate the catalytic activity and coke resistance during DRM. The prepared core@shell $Ni@Co_x$ NPs were supported on CeO_2. As-prepared core@shell $Ni@Co_x$ NPs were supported on CeO_2 and alloyed bimetallic $Ni–Co_x$ NPs on CeO_2 were also fabricated for comparison. Both catalysts significantly mitigate coke deposition with increasing amounts of Co, but overall the $Ni@Co_x/CeO$ catalyst exhibits higher DRM activity. However, the activity of the $Ni@Co_x/CeO_2$ catalyst rapidly decreased to less than half when the Co/Ni ratio exceeded 1. The $Ni@Co_1/CeO_2$ catalyst showed the highest CH_4 and CO_2 conversions among the series of $NiCo_x/CeO_2$ catalysts and long-term stability without deactivation at 800 °C. After the DRM at 800 °C for 10 h, the initial core@shell NP of the $Ni@Co_1/CeO_2$ catalyst lost the Co shell and changed to a homogeneous alloy. However, the bimetallic alloyed $Ni–Co_1/CeO_2$ catalyst became a non-uniform alloy with a high fraction of Co exposed on the surface after the long-term DRM for 10 h. Although both catalysts undergo structural changes by Ni and Co diffusion during the DRM, the core@shell $Ni@Co_1/CeO_2$ catalyst exhibited more stable catalytic activity than the randomly alloyed bimetallic $Ni–Co_1/CeO_2$ catalyst. It was confirmed that the $Ni@Co_1/CeO_2$ catalyst is effective in rapidly forming a uniform alloy at the initial stage of the DRM reaction and exhibits excellent and stable catalytic performance. When $Ni@Co_1$ NPs were supported on Al_2O_3 or SiO_2, the CH_4 conversion significantly reduced, indicating that CeO_2 with abundant oxygen vacancies plays an important role during the DRM. H_2-TPR results confirmed that the interaction between Ni and CeO_2 became stronger as the Co content increased. XPS further confirmed that surfaces oxygen adsorbed on Co species increased, as the amount of Co increased in the $Ni@Co_x/CeO_2$ catalyst. The CO_2-TPD results showed that Co metal mainly contributes to the improved CO_2

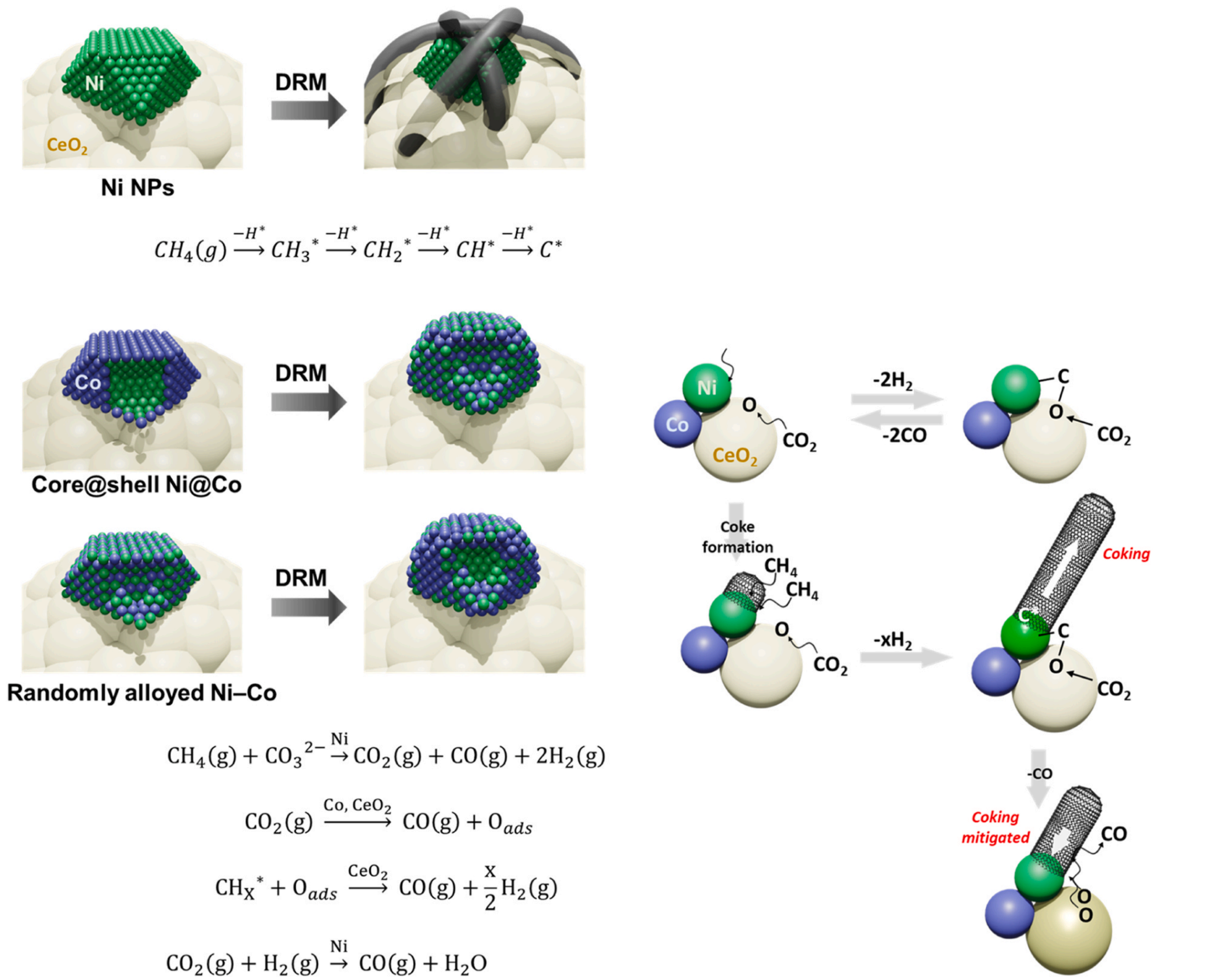

Scheme 1. Proposed mechanisms for coke formation and relaxation during DRM for bare Ni, core@shell Ni@Co_1, and randomly alloyed Ni–Co_1 NP catalysts supported on CeO_2.

adsorption to CeO_2. It was concluded that CeO_2 together with Co plays an important role by removing carbon species generated on the Ni surface and releasing CO. The synergistic effect of the additional Co shell and reducible CeO_2 in the core@shell Ni@Co_x NPs greatly enhances the DRM performance and effectively inhibits carbon coking.

Author statement

The manuscript was written with contributions from all authors. All the authors approved the final version of the manuscript.

CRediT authorship contribution statement

E.Y and **E.N** performed experiments, characterized catalysts, and analyzed data. **Y.J.** performed characterization and drawing figure arts. **K.A** supervised the study and edited the manuscript. All authors discussed the results and commented on the manuscript. The manuscript was written with contributions from all authors. All the authors approved the final version of the manuscript. **E.Y** and **E.N** contributed equally to this work as the first author.

Declaration of Competing Interest

The authors declare that they have no known competing financial interests or personal relationships that could have appeared to influence the work reported in this paper.

Data availability

No data was used for the research described in the article.

Acknowledgements

This research was supported by the Basic Science Research Program (2021R1A2C2006713), Engineering Research Center of Excellence Program (2020R1A5A1019631), Climate Environment R&D Program (2022M3J1A1052840), and Regional Innovation Strategy (RIS) (2021RIS-003) of the National Research Foundation of Korea (NRF) funded by the Ministry of Science and ICT, Ministry of Education (MOE), and Technology Innovation Program (20012971, 20010853) by the Ministry of Trade, Industry & Energy (MOTIE).

Appendix A. Supporting information

Characterization details; reaction results; TEM, HAADF-STEM, ICP–OES and XPS data of Ni@Co/CeO_2 catalysts. Supplementary data associated with this article can be found in the online version at doi:10.1016/j.apcatb.2023.123152.

References

[1] Z. Bian, Z. Wang, B. Jiang, P. Hongmanorom, W. Zhong, S. Kawi, A review on perovskite catalysts for reforming of methane to hydrogen production, Renew. Sustain. Energy Rev. 134 (2020), 110291.

[2] Z. Bian, I.Y. Suryawinata, S. Kawi, Highly carbon resistant multicore-shell catalyst derived from Ni-Mg phyllosilicate nanotubes@silica for dry reforming of methane, Appl. Catal., B 195 (2016) 1–8.

[3] S. van Renssen, The hydrogen solution? Nat. Clim. Chang. 10 (2020) 799–801.

[4] Z. Li, B. Jiang, Z. Wang, S. Kawi, High carbon resistant Ni@Ni phyllosilicate@SiO_2 core shell hollow sphere catalysts for low temperature CH_4 dry reforming, J. CO_2 Util. 27 (2018) 238–246.

[5] Z. Li, Q. Lin, M. Li, J. Cao, F. Liu, H. Pan, Z. Wang, S. Kawi, Recent advances in process and catalyst for CO_2 reforming of methane, Renew. Sustain. Energy Rev. 134 (2020), 110312.

[6] Z. Bian, S. Kawi, Sandwich-like silica@Ni@silica multicore–shell catalyst for the low-temperature dry reforming of methane: confinement effect against carbon formation, ChemCatChem 10 (2018) 320–328.

[7] Z. Li, Y. Kathiraser, J. Ashok, U. Oemar, S. Kawi, Simultaneous tuning porosity and basicity of nickel@nickel-magnesium phyllosilicate core-shell catalysts for CO_2 reforming of CH_4, Langmuir 30 (2014) 14694–14705.

[8] Y.X. Yu, J. Yang, K.K. Zhu, Z.J. Sui, D. Chen, Y.A. Zhu, X.G. Zhou, High-throughput screening of alloy catalysts for dry methane reforming, ACS Catal. 11 (2021) 8881–8894.

[9] P.G. Lustemberg, Z. Mao, A. Salcedo, B. Irigoyen, M.V. Ganduglia-Pirovano, C. T. Campbell, Nature of the active sites on Ni/CeO_2 catalysts for methane conversions, ACS Catal. 11 (2021) 10604–10613.

[10] X. Gao, J. Ashok, S. Kawi, Smart designs of anti-coking and anti-sintering ni-based catalysts for dry reforming of methane: a recent review, Reactions 1 (2020) 162–194.

[11] S. Dama, S.R. Ghodke, R. Bobade, H.R. Gurav, S. Chilukuri, Active and durable alkaline earth metal substituted perovskite catalysts for dry reforming of methane, Appl. Catal. B 224 (2018) 146–158.

[12] Z. Li, Z. Wang, B. Jiang, S. Kawi, Sintering resistant Ni nanoparticles exclusively confined within SiO_2 nanotubes for CH_4 dry reforming, Catal. Sci. Technol. 8 (2018) 3363–3371.

[13] Z. Bian, W. Zhong, Y. Yu, Z. Wang, B. Jiang, S. Kawi, Dry reforming of methane on Ni/mesoporous-Al2O3 catalysts: effect of calcination temperature, Int. J. Hydrog. Energy 46 (2021) 31041–31053.

[14] S. Das, S. Bhattar, L. Liu, Z. Wang, S. Xi, J.J. Spivey, S. Kawi, Effect of partial fe substitution in $La_{0.9}Sr_{0.1}NiO_3$ perovskite-derived catalysts on the reaction mechanism of methane dry reforming, ACS Catal. 10 (2020) 12466–12486.

[15] J. Lu, B. Fu, M.C. Kung, G. Xiao, J.W. Elam, H.H. Kung, P.C. Stair, Coking- and sintering-resistant palladium catalysts achieved through atomic layer deposition, Science 335 (2012) 1205–1208.

[16] M. Wolf, Thermodynamic assessment of the stability of bulk and nanoparticulate cobalt and nickel during dry and steam reforming of methane, RSC Adv. 11 (2021) 18187–18197.

[17] S. Li, J. Gong, Strategies for improving the performance and stability of Ni-based catalysts for reforming reactions, Chem. Soc. Rev. 43 (2014) 7245–7256.

[18] Q. Zhou, X. Fu, K. Hui Lim, Z. Li, M. Liao, J. Lu, F. Liu, S. Kawi, Complete confinement of Ce/Ni within SiO_2 nanotube with high oxygen vacancy concentration for CO_2 methane reforming, Fuel 325 (2022), 124819.

[19] M. Liao, Y. Chen, M. Chen, K.H. Lim, Z. Li, H. Wu, X. He, Q. Zhou, S. Kawi, CeO_2 Nanorod@NiPhy core-shell catalyst for methane dry reforming: effect of simultaneous sintering prevention of CeO_2 support and active Ni, ChemCatChem 14 (2022), e202200762.

[20] X. Gao, Z. Ge, G. Zhu, Z. Wang, J. Ashok, S. Kawi, Anti-coking and anti-sintering Ni/Al_2O_3 catalysts in the dry reforming of methane: recent progress and prospects, Catalysts 11 (2021) 1003.

[21] S. Chen, J. Zaffran, B. Yang, Descriptor design in the computational screening of Ni-based catalysts with balanced activity and stability for dry reforming of methane reaction, ACS Catal. 10 (2020) 3074–3083.

[22] K.Y. Kim, J.H. Lee, H. Lee, W.Y. Noh, E.H. Kim, E.C. Ra, S.K. Kim, K. An, J.S. Lee, Layered double hydroxide-derived intermetallic $Ni_3GaC_{0.25}$catalysts for dry reforming of methane, ACS Catal. 11 (2021) 11091–11102.

[23] Z. Bian, S. Kawi, Highly carbon-resistant Ni-Co/SiO_2 catalysts derived from phyllosilicates for dry reforming of methane, J. CO_2 Util. 18 (2017) 345–352.

[24] B. Yan, X. Yang, S. Yao, J. Wan, M.N.Z. Myint, E. Gomez, Z. Xie, S. Kattel, W. Xu, J. G. Chen, Dry reforming of ethane and butane with CO_2 over PtNi/CeO_2 bimetallic catalysts, ACS Catal. 6 (2016) 7283–7292.

[25] Y. Xiong, L. Xiao, Y. Yang, F.J. Disalvo, H.D. Abruña, High-loading intermetallic Pt_3Co/C core-shell nanoparticles as enhanced activity electrocatalysts toward the oxygen reduction reaction (ORR), Chem. Mater. 30 (2018) 1532–1539.

[26] X. Ao, W. Zhang, B. Zhao, Y. Ding, G. Nam, L. Soule, A. Abdelhafiz, C. Wang, M. Liu, Atomically dispersed Fe-N-C decorated with Pt-alloy core-shell nanoparticles for improved activity and durability towards oxygen reduction, Energy Environ. Sci. 13 (2020) 3032–3040.

[27] R.T. Hannagan, G. Giannakakis, M. Flytzani-Stephanopoulos, E.C.H. Sykes, Single-atom alloy catalysis, Chem. Rev. 120 (2020) 12044–12088.

[28] J. Niu, Y. Wang, S.E. Liland, S. K. Regli, J. Yang, K.R. Rout, J. Luo, M. Rønning, J. Ran, D. Chen, Unraveling enhanced activity, selectivity, and coke resistance of Pt-Ni bimetallic clusters in dry reforming, ACS Catal. 11 (2021) 2398–2411.

[29] Z. Li, M. Li, Z. Bian, Y. Kathiraser, S. Kawi, Design of highly stable and selective core/yolk-shell nanocatalysts-review, Appl. Catal. B 188 (2016) 324–341.

[30] Z. Li, Z. Wang, S. Kawi, Sintering and coke resistant core/yolk shell catalyst for hydrocarbon reforming, ChemCatChem 11 (2019) 202–224.

[31] H.O. Otor, J.B. Steiner, C. García-Sancho, A.C. Alba-Rubio, Encapsulation methods for control of catalyst deactivation: a review, ACS Catal. 10 (2020) 7630–7656.

[32] S. Das, J. Pérez-Ramírez, J. Gong, N. Dewangan, K. Hidajat, B.C. Gates, S. Kawi, Core-shell structured catalysts for thermocatalytic, photocatalytic, and electrocatalytic conversion of CO_2, Chem. Soc. Rev. 49 (2020) 2937–3004.

[33] Z. Li, Y. Kathiraser, S. Kawi, Facile synthesis of high surface area yolk-shell Ni@Ni embedded SiO_2 via Ni phyllosilicate with enhanced performance for CO_2 reforming of CH_4, ChemCatChem 7 (2015) 160–168.

[34] Z. Li, S. Kawi, Multi-Ni@Ni phyllosilicate hollow sphere for CO_2 reforming of CH_4: influence of Ni precursors on structure, sintering, and carbon resistance, Catal. Sci. Technol. 8 (2018) 1915–1922.

[35] E. Yang, E. Nam, J. Lee, H. Lee, E.D. Park, H. Lim, K. An, Al_2O_3-coated Ni/CeO_2 nanoparticles as coke-resistant catalyst for dry reforming of methane, Catal. Sci. Technol. 10 (2020) 8283–8294.

[36] M. Kosari, S. Askari, A.M. Seayad, S. Xi, S. Kawi, A. Borgna, H.C. Zeng, Strong coke-resistivity of spherical hollow Ni/SiO_2 catalysts with shell-confined high-content Ni nanoparticles for methane dry reforming with CO_2, Appl. Catal., B 310 (2022), 121360.

[37] Y. Tang, Y. Wei, Z. Wang, S. Zhang, Y. Li, L. Nguyen, Y. Li, Y. Zhou, W. Shen, F. F. Tao, P. Hu, Synergy of single-atom Ni1 and Ru1 sites on CeO_2 for dry reforming of CH_4, J. Am. Chem. Soc. 141 (2019) 7283–7293.

[38] M. Akri, S. Zhao, X. Li, K. Zang, A.F. Lee, M.A. Isaacs, W. Xi, Y. Gangarajula, J. Luo, Y. Ren, Y.T. Cui, L. Li, Y. Su, X. Pan, W. Wen, Y. Pan, K. Wilson, L. Li, B. Qiao, H. Ishii, Y.F. Liao, A. Wang, X. Wang, T. Zhang, Atomically dispersed nickel as coke-resistant active sites for methane dry reforming, Nat. Commun. 10 (2019) 5181.

[39] S. Das, A. Jangam, S. Jayaprakash, S. Xi, K. Hidajat, K. Tomishige, S. Kawi, Role of lattice oxygen in methane activation on Ni-phyllosilicate@$Ce_{1-x}Zr_xO_2$ core-shell catalyst for methane dry reforming: Zr doping effect, mechanism, and kinetic study, Appl. Catal. B 290 (2021), 119998.

[40] Z. Liu, D.C. Grinter, P.G. Lustemberg, T. Nguyen-Phan, Y. Zhou, S. Luo, I. Waluyo, E.J. Crumlin, D.J. Stacchiola, J. Zhou, J. Carrasco, H.F. Busnengo, M.V. Ganduglia-Pirovano, S.D. Senanayake, J.A. Rodriguez, Dry reforming of methane on a highly-active Ni-CeO_2 catalyst: effects of metal-support interactions on C−H bond breaking, Angew. Chem. 128 (2016) 7581–7585.

[41] P.G. Lustemberg, P.J. Ramírez, Z. Liu, R.A. Gutiérrez, D.G. Grinter, J. Carrasco, S. D. Senanayake, J.A. Rodriguez, M.V. Ganduglia-Pirovano, Room-temperature activation of methane and dry re-forming with CO_2 on Ni-CeO_2 (111) surfaces: effect of Ce^{3+} sites and metal-support interactions on C-H bond cleavage, ACS Catal. 6 (2016) 8184–8191.

[42] Z. Li, K. Sibudjing, Facile synthesis of multi-Ni-core@Ni phyllosilicate@CeO_2 shell hollow spheres with high oxygen vacancy concentration for dry reforming of CH_4, ChemCatChem 10 (2018) 2994–3001.

[43] M. Li, Z. Li, Q. Lin, J. Cao, F. Liu, M.H. Wai, S. Kawi, Sintering resistant cubic ceria yolk Ni phyllosilicate shell catalyst for methane dry reforming, Catal. Today 402 (2022) 319–327.

[44] J. Zhang, H. Wang, A.K. Dalai, Development of stable bimetallic catalysts for carbon dioxide reforming of methane, J. Catal. 249 (2007) 300–310.

[45] S. De, J. Zhang, R. Luque, N. Yan, Ni-based bimetallic heterogeneous catalysts for energy and environmental applications, Energy Environ. Sci. 9 (2016) 3314–3347.

[46] Z. Li, M. Li, J. Ashok, S. Kawi, NiCo@NiCo phyllosilicate@CeO_2 hollow core shell catalysts for steam reforming of toluene as biomass tar model compound, Energy Convers. Manag. 180 (2019) 822–830.

[47] S. Das, K.H. Lim, T.Z.H. Gani, S. Aksari, S. Kawi, Bi-functional CeO_2 coated NiCo-MgAl core-shell catalyst with high activity and resistance to coke and H_2S poisoning in methane dry reforming, Appl. Catal. B 323 (2023).

[48] W. Tu, M. Ghoussoub, C.V. Singh, Y.H.C. Chin, Consequences of surface oxophilicity of Ni, Ni-Co, and Co clusters on methane activation, J. Am. Chem. Soc. 139 (2017) 6928–6945.

[49] K. Takanabe, K. Nagaoka, K. Nariai, K.I. Aika, Titania-supported cobalt and nickel bimetallic catalysts for carbon dioxide reforming of methane, J. Catal. 232 (2005) 268–275.

[50] K. Cao, M. Gong, J. Yang, J. Cai, S. Chu, Z. Chen, B. Shan, R. Chen, Nickel catalyst with atomically-thin meshed cobalt coating for improved durability in dry reforming of methane, J. Catal. 373 (2019) 351–360.

[51] S. Zhang, L. Nguyen, J.X. Liang, J. Shan, J.J. Liu, A.I. Frenkel, A. Patlolla, W. Huang, J. Li, F.F. Tao, Catalysis on singly dispersed bimetallic sites, Nat. Commun. 6 (2015).

[52] I.V. Yentekakis, P. Panagiotopoulou, G. Artemakis, A review of recent efforts to promote dry reforming of methane (DRM) to syngas production via bimetallic catalyst formulations, Appl. Catal. B 296 (2021), 120210.

[53] Y. Yang, Y.A. Lin, X. Yan, F. Chen, Q. Shen, L. Zhang, N. Yan, Cooperative atom motion in Ni-Cu nanoparticles during the structural evolution and the implication in the high-temperature catalyst design, ACS Appl. Energy Mater. 2 (2019) 8894–8902.

[54] T.S. Phan, A.R. Sane, B. Rêgo de Vasconcelos, A. Nzihou, P. Sharrock, D. Grouset, D. Pham Minh, Hydroxyapatite supported bimetallic cobalt and nickel catalysts for syngas production from dry reforming of methane, Appl. Catal. B 224 (2018) 310–321.

[55] S. Carenco, C.H. Wu, A. Shavorskiy, S. Alayoglu, G.A. Somorjai, H. Bluhm, M. Salmeron, Synthesis and structural evolution of nickel-cobalt nanoparticles under H_2 and CO_2, Small 11 (2015) 3045–3053.

[56] N. Musselwhite, K. Na, S. Alayoglu, G.A. Somorjai, The pathway to total isomer selectivity: N-hexane conversion (reforming) on platinum nanoparticles supported

on aluminum modified mesoporous silica (MCF-17), J. Am. Chem. Soc. 136 (2014) 16661–16665.
[57] V. Iablokov, S.K. Beaumont, S. Alayoglu, V.V. Pushkarev, C. Specht, J. Gao, A. P. Alivisatos, N. Kruse, G.A. Somorjai, Size-controlled model Co nanoparticle catalysts for CO_2 hydrogenation: synthesis, characterization, and catalytic reactions, Nano Lett. 12 (2012) 3091–3096.
[58] Z. Li, S. Das, P. Hongmanorom, N. Dewangan, M.H. Wai, S. Kawi, Silica-based micro- and mesoporous catalysts for dry reforming of methane, Catal. Sci. Technol. 8 (2018) 2763–2778.
[59] S. Das, J. Ashok, Z. Bian, N. Dewangan, M.H. Wai, Y. Du, A. Borgna, K. Hidajat, S. Kawi, Silica–Ceria sandwiched Ni core–shell catalyst for low temperature dry reforming of biogas: coke resistance and mechanistic insights, Appl. Catal. B 230 (2018) 220–236.
[60] K. Sheng, D. Luan, H. Jiang, F. Zeng, B. Wei, F. Pang, J. Ge, Ni_xCo_y nanocatalyst supported by ZrO_2 hollow sphere for dry reforming of methane: synergetic catalysis by Ni and Co in alloy, ACS Appl. Mater. Interfaces 11 (2019) 24078–24087.
[61] R.P. Ye, Q. Li, W. Gong, T. Wang, J.J. Razink, L. Lin, Y.Y. Qin, Z. Zhou, H. Adidharma, J. Tang, A.G. Russell, M. Fan, Y.G. Yao, High-performance of nanostructured Ni/CeO_2 catalyst on CO_2 methanation, Appl. Catal. B 268 (2020), 118474.
[62] W. Shan, M. Luo, P. Ying, W. Shen, C. Li, Reduction property and catalytic activity of $Ce_{1-X}Ni_XO_2$ mixed oxide catalysts for CH_4 oxidation, Appl. Catal. A 246 (2003) 1–9.
[63] P. Hongmanorom, J. Ashok, P. Chirawatkul, S. Kawi, Interfacial synergistic catalysis over Ni nanoparticles encapsulated in mesoporous ceria for CO_2 methanation, Appl. Catal. B 297 (2021), 120454.
[64] N. Rui, X. Zhang, F. Zhang, Z. Liu, X. Cao, Z. Xie, R. Zou, S.D. Senanayake, Y. Yang, J.A. Rodriguez, C.J. Liu, Highly active Ni/CeO_2 catalyst for CO_2 methanation: preparation and characterization, Appl. Catal. B 282 (2021), 119581.
[65] L. Xu, Y. Cui, M. Chen, X. Wen, C. Lv, X. Wu, C.E. Wu, Z. Miao, X. Hu, Screening transition metals (Mn, Fe, Co, and Cu) promoted Ni-based CO_2 methanation bimetal catalysts with advanced low-temperature activities, Ind. Eng. Chem. Res. 60 (2021) 8056–8072.
[66] A.H. Braga, D.C. De Oliveira, A.R. Taschin, J.B.O. Santos, J.M.R. Gallo, J.M. C. Buen, Steam reforming of ethanol using Ni-Co catalysts supported on $MgAl_2O_4$: structural study and catalytic properties at different temperatures, ACS Catal. 11 (2021) 2047–2061.
[67] C.O. Calgaro, O.W. Perez-Lopez, Biogas dry reforming for hydrogen production over Ni-M-Al catalysts (M = Mg, Li, Ca, La, Cu, Co, Zn), Int. J. Hydrog. Energy 44 (2019) 17750–17766.
[68] M. Zhang, J. Zhang, Z. Zhou, S. Chen, T. Zhang, F. Song, Q. Zhang, N. Tsubaki, Y. Tan, Y. Han, Effects of the surface adsorbed oxygen species tuned by rare-earth metal doping on dry reforming of methane over Ni/ZrO_2 catalyst, Appl. Catal., B 264 (2020), 118522.
[69] Y. Zhao, F. Dong, W. Han, H. Zhao, Z. Tang, Construction of Cu-Ce/graphene catalysts via a one-step hydrothermal method and their excellent CO catalytic oxidation performance, RSC Adv. 8 (2018) 1583–1592.
[70] Y. Turap, I. Wang, T. Fu, Y. Wu, Y. Wang, W. Wang, Co–Ni alloy supported on CeO_2 as a bimetallic catalyst for dry reforming of methane, Int. J. Hydrog. Energy 45 (2020) 6538–6548.
[71] B. AlSabban, L. Falivene, S.M. Kozlov, A. Aguilar-Tapia, S. Ould-Chikh, J. L. Hazemann, L. Cavallo, J.M. Basset, K. Takanabe, In-operando elucidation of bimetallic CoNi nanoparticles during high-temperature CH_4/CO_2 reaction, Appl. Catal. B 213 (2017) 177–189.
[72] Z. Wu, B. Yang, S. Miao, W. Liu, J. Xie, S. Lee, M.J. Pellin, D. Xiao, D. Su, D. Ma, Lattice strained Ni-Co alloy as a high-performance catalyst for catalytic dry reforming of methane, ACS Catal. 9 (2019) 2693–2700.
[73] J. Wang, Y. Fu, W. Kong, S. Li, C. Yuan, J. Bai, X. Chen, J. Zhang, Y. Sun, Investigation of atom-level reaction kinetics of carbon-resistant bimetallic NiCo-reforming catalysts: combining microkinetic modeling and density functional theory, ACS Catal. 12 (2022) 4382–4393.
[74] S. Das, M. Sengupta, A. Bag, M. Shah, A. Bordoloi, Facile synthesis of highly disperse Ni-Co nanoparticles over mesoporous silica for enhanced methane dry reforming, Nanoscale 10 (2018) 6409–6425.
[75] S. Zhang, S. Muratsugu, N. Ishiguro, M. Tada, Ceria-doped Ni/SBA-16 catalysts for dry reforming of methane, ACS Catal. 3 (2013) 1855–1864.
[76] C.G. Anchieta, E.M. Assaf, J.M. Assaf, Syngas production by methane tri-reforming: effect of Ni/CeO_2 synthesis method on oxygen vacancies and coke formation, J. CO_2 Util. 56 (2022), 101853.